

Measurement of fast bars in a sample of early-type barred galaxies

J. A. L. Aguerri,^{1,2}★ Victor P. Debattista² and Enrico Maria Corsini³

¹Instituto de Astrofísica de Canarias, Vía Láctea s/n. E-38200 La Laguna, Spain

²Astronomisches Institut, Universität Basel, Venusstrasse 7, CH-4102 Binningen, Switzerland

³Dipartimento di Astronomia, Università di Padova, vicolo dell’Osservatorio 2, I-35122 Padova, Italy

Accepted 2002 September 12. Received 2002 September 9; in original form 2002 July 31

ABSTRACT

We present surface photometry and stellar kinematics of a sample of five SB0 galaxies: ESO 139-G009, IC 874, NGC 1308, NGC 1440 and NGC 3412. We measured their bar pattern speed using the Tremaine–Weinberg method, and derived the ratio, \mathcal{R} , of the corotation radius to the length of the bar semimajor axis. For all the galaxies, \mathcal{R} is consistent with being in the range from 1.0 to 1.4, i.e. that they host fast bars. This represents the largest sample of galaxies for which \mathcal{R} has been measured in this way. Taking into account the measured distribution of \mathcal{R} and our measurement uncertainties, we argue that this is probably the true distribution of \mathcal{R} . If this is the case, then the Tremaine–Weinberg method finds a distribution of \mathcal{R} which is in agreement with that obtained by hydrodynamical simulations. We compare this result with recent high-resolution N -body simulations of bars in cosmologically motivated dark matter haloes, and we conclude that these bars are not located inside centrally concentrated dark matter haloes.

Key words: galaxies: elliptical and lenticular, cD – galaxies: haloes – galaxies: kinematics and dynamics – galaxies: photometry.

1 INTRODUCTION

The pattern speed of a bar, Ω_p , is its main kinematic observable. When parametrized by the distance-independent ratio $\mathcal{R} \equiv D_L/a_B$ (where D_L is the Lagrangian/corotation radius, at which a star is at rest in the bar’s rest frame, and a_B is the bar’s semimajor axis), it permits the classification of bars into fast ($1.0 \leq \mathcal{R} \leq 1.4$) and slow ($\mathcal{R} > 1.4$) bars. If $\mathcal{R} < 1.0$, orbits are elongated perpendicular to the bar, so that self-consistent bars cannot exist in this regime (Contopoulos 1980).

A robust method for measuring \mathcal{R} relies on hydrodynamical simulations to model gas, particularly at shocks. These studies find fast bars (e.g. Lindblad, Lindblad & Athanassoula 1996; Lindblad & Kristen 1996; Weiner, Sellwood & Williams 2001). Hydrodynamical simulations can also obtain \mathcal{R} by matching morphological features in H α (e.g. Laine 1996; England, Gottesman & Hunter 1990; Hunter et al. 1989; Aguerri et al. 2001). Moreover, if the leading, offset dust lanes frequently found in bars can be identified with shocks, then fast bars seem to be the norm in late-type galaxies (van Albada & Sanders 1982; Athanassoula 1992). A model-independent method for measuring Ω_p directly was obtained by Tremaine & Weinberg (1984). The Tremaine–Weinberg (TW) method is given by the simple expression $\mathcal{X}\Omega_p \sin i = \mathcal{V}$, where \mathcal{X} and \mathcal{V} are the luminosity-weighted mean position and velocity

measured along slits parallel to the line of nodes. If a number of slits at different offsets from the major axis are obtained for a galaxy, then plotting \mathcal{V} versus \mathcal{X} for the different slits produces a straight line with slope $\Omega_p \sin i$. To date, this method has been applied successfully to three early-type barred galaxies (Kent 1987; Merrifield & Kuijken 1995; Gerssen, Kuijken & Merrifield 1999; Debattista, Corsini & Aguerri 2002) and preliminary results have been obtained for another five galaxies ranging from SB0 to SBb (Debattista & Williams 2001; Gerssen 2002). Although all these galaxies are consistent with having fast bars, the sample size is still small enough that the range of \mathcal{R} recovered by the TW method is still poorly defined. We have started a program to enlarge the sample of pattern speeds measured with the TW method, including galaxies of various bar strength, environment, luminosity, inclination, etc. In a previous paper, (Debattista et al. 2002, hereafter Paper I), we reported on the special case of NGC 1023, a system which shows evidence of a past interaction with one or more of its satellite galaxies. In this paper, we present results for an additional five SB0 galaxies.

2 THE SAMPLE

Our preliminary sample of galaxies consisted of 11 SB0 objects selected to be bright and undisturbed, with no evidence of dust or spiral arms to complicate the TW analysis, generally not too many nearby stars, and a bar at an angle intermediate between the orientation of the major and minor axes. After detailed analysis of their photometrical properties (as described in Section 3 below),

★E-mail: jalfonso@ii.iac.es (JALA); corsini@pd.astro.it (EMC)

Table 1. Parameters of the sample galaxies. The columns show the following: (2) morphological classification from de Vaucouleurs et al. (1991, hereafter RC3); (3) galaxy inclination from $\log R_{25}$ in RC3; (4) major-axis position angle from RC3, except for NGC 1308 and 3412 (LEDA); (5) total observed blue magnitude from LEDA; (6) apparent isophotal diameters measured at a surface-brightness level of $\mu_B = 25 \text{ mag arcsec}^{-2}$ from RC3; (7) radial velocity with respect to the CMB radiation from RC3, except for NGC 1308 (LEDA); (8) distance obtained as V_{CBR}/H_0 with $H_0 = 75 \text{ km s}^{-1} \text{ Mpc}^{-1}$; (9) absolute total blue magnitude from M_B corrected for inclination and extinction as in LEDA and adopting D .

Galaxy	Type	i	PA	B_T	$D_{25} \times d_{25}$	V_{CBR}	D	$M_{B_T}^0$
(1)	(RC3)	(°)	(°)	(mag)	(arcsec)	(km s $^{-1}$)	(Mpc)	(mag)
	(2)	(3)	(4)	(5)	(6)	(7)	(8)	(9)
ESO 139-G009	(R)SAB0(rs)	$43.6^{+5.1}_{-6.2}$	94	14.35	74×60	5389	71.9	-20.28
IC 874	SB0(rs)	$35.6^{+5.0}_{-6.2}$	17	13.60	60×43	2602	34.7	-19.41
NGC 1308	SB0(r)	$43.6^{+0.2}_{-8.0}$	135	14.70	70×51	6180	82.4	-19.88
NGC 1440	(R')SB0(rs)	$40.7^{+4.3}_{-5.0}$	28	12.90	128×97	1382	18.4	-18.90
NGC 3412	SB0(s)	$55.8^{+2.6}_{-2.8}$	155	11.43	218×123	1202	16.0	-19.73

five of them were rejected either because of strong variation in the ellipticity and/or position angle of the isophotal profiles at large galactocentric distances, or because of the presence of dust in their inner regions. Of the remaining six, we studied one of them, NGC 1023, in Paper I; in this paper we will analyse the remaining five galaxies: ESO 139-G009 (SAB0), IC 874 (SB0), NGC 1308 (SB0), NGC 1440 (SB0) and NGC 3412 (SB0). A compilation of their properties from the literature is given in Table 1.

Four of these galaxies, ESO 139-G009, IC 874, NGC 1308 and NGC 1440, were previously poorly studied. Indeed, no surface photometry or stellar kinematics were available for the first three of these, and only V -band photometry was available for NGC 1440 (Kodaira, Okamura & Ichikawa 1990), from which Baggett, Baggett & Anderson (1998) obtained a decomposition into bulge and disc.

This was not the case for NGC 3412, for which both surface photometry and stellar kinematics were available. Optical and near-infrared (NIR) imaging of NGC 3412 were obtained by Kent (1984, r), Kodaira et al. (1990, V), Shaw et al. (1995 JHK) and Ann (2001 $UBVRI$ and $H\alpha$). Both Shaw et al. (1995) and Ann (2001) measured an isophotal twist in the nuclear region of this galaxy, suggesting that its bulge is triaxial. Bulge–disc decompositions were performed by Kent (1985, r) and Baggett et al. (1998, V). Kuijken, Fisher & Merrifield (1996) obtained the position-velocity diagram of the stellar component along $\text{PA} = 155^\circ$ (the ‘major axis’, but see our discussion in Section 3) of NGC 3412, to search for counter-rotation. They found that the fraction of counter-rotating disc stars is less than 5 per cent. Spatially resolved stellar kinematics of this galaxy have been measured by Fisher (1997, $\text{PA} = 55^\circ, 155^\circ$) and Neistein et al. (1999, $\text{PA} = 155^\circ$), who derived the Tully–Fisher relation for a sample of nearby lenticular galaxies.

3 SURFACE PHOTOMETRY

The photometric observations of ESO 139-G009 and IC 874 were carried out with the 3.5-m New Technology Telescope (NTT) at the European Southern Observatory (ESO) in La Silla (Chile) in 2001 May. We used the ESO Multi-Mode Instrument (EMMI) in red imaging and low-dispersion spectroscopic (RILD) mode. The detector was the No 36 Tektronik TK2048 EB CCD with 2048×2048 pixels. The image scale was $0.27 \text{ arcsec pixel}^{-1}$. We imaged NGC 1308 and 3412 at the 1-m Jacobus Kapteyn Telescope located at the Roque de los Muchachos Observatory (ORM) in La Palma (Spain) in 2001 October and 2000 May, respectively. We used a SITe2 CCD

Table 2. Log of the photometrical observations.

Galaxy	Date	Exp. Time (s)		
		B	V	I
ESO 139-G009	2001 May 22–23	1440 ^a	480 ^a	300 ^b
IC 874	2001 May 22–23	600 ^a		300 ^b
NGC 1308	2001 Oct 11			7200 ^c
NGC 1440	2001 Nov 11	2400 ^a		3600 ^b
NGC 3412	2000 May 27–28	2400 ^c	2700 ^c	3600 ^c

NOTE: ^aBessel, ^bGunn, ^cHarris.

with 2048×2048 pixels and an image scale of $0.33 \text{ arcsec pixel}^{-1}$. Finally, we observed NGC 1440 with the Danish 1.54-m telescope at ESO in La Silla in 2001 November. The telescope mounted the Danish Faint Object Spectrograph and Camera (DFOSC) with the EEV/MAT 44–82 CCD with 2048×4096 pixels. The image scale was $0.39 \text{ arcsec pixel}^{-1}$. The log of the photometrical observations is given in Table 2.

All images were reduced using standard IRAF¹ tasks. First, we subtracted a bias frame consisting of 10 exposures for each night. The images were then flat-fielded using sky flats taken at twilight. The sky-background level was removed by fitting a second-order polynomial to the regions free of sources in the images. Special care was taken at this point to obtain a final background in the images free of sources, in order to reach the outermost parts of the objects. Cosmic rays were removed by combining the different exposures for each filter using a sigma clipping rejection algorithm.

Photometric calibrations were achieved by means of standard stars. The calibration constants include corrections for atmospheric and Galactic extinction, and a colour term. Fig. 1 shows calibrated I -band images of the galaxies.

4 BAR LENGTH

4.1 Photometrical parameters

Isophote-fitting with ellipses, after masking foreground stars and bad pixels, was carried out using the IRAF task ELLIPSE. In all cases, we first fit ellipses allowing their centres to vary; within the errors, no variation in the ellipse centres was found for the five galaxies

¹ IRAF is distributed by NOAO, which is operated by AURA Inc., under contract with the National Science Foundation.

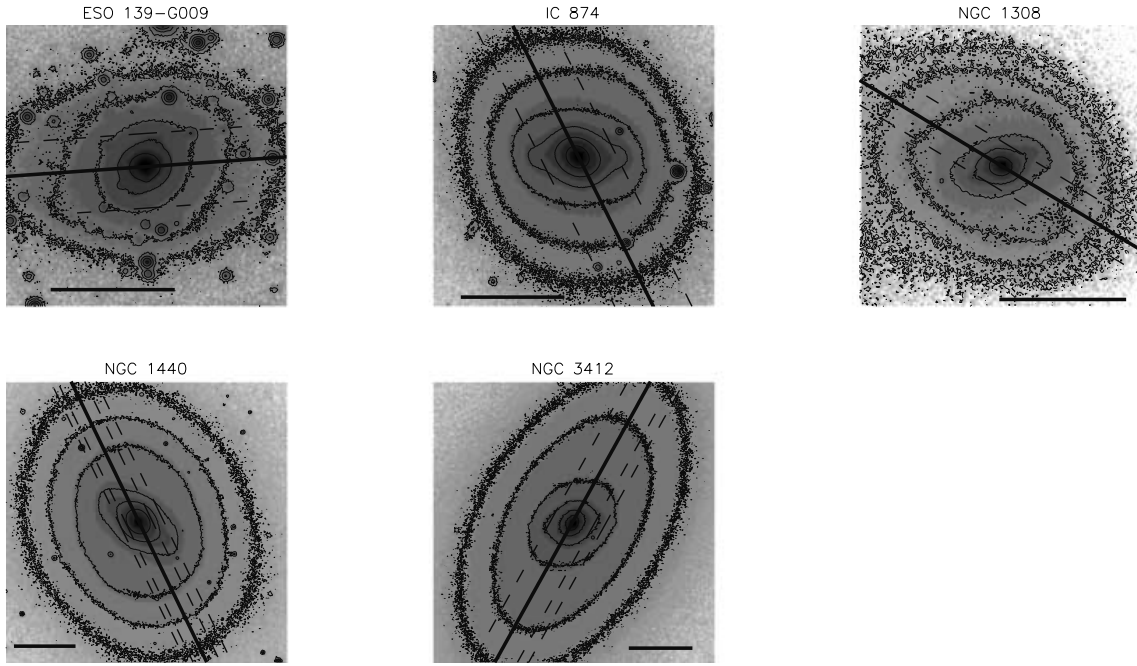


Figure 1. I -band images of the sample galaxies. The isocontours are spaced at $1 \text{ mag arcsec}^{-2}$ and the outermost corresponds to $\mu_I = 23 \text{ mag arcsec}^{-2}$. In each panel, North is up and East is left, and the bottom horizontal line is 30 arcsec long. For each galaxy, the thick continuous line and the dashed lines show the slit position along major axis and the offsets in the spectroscopic observations, respectively.

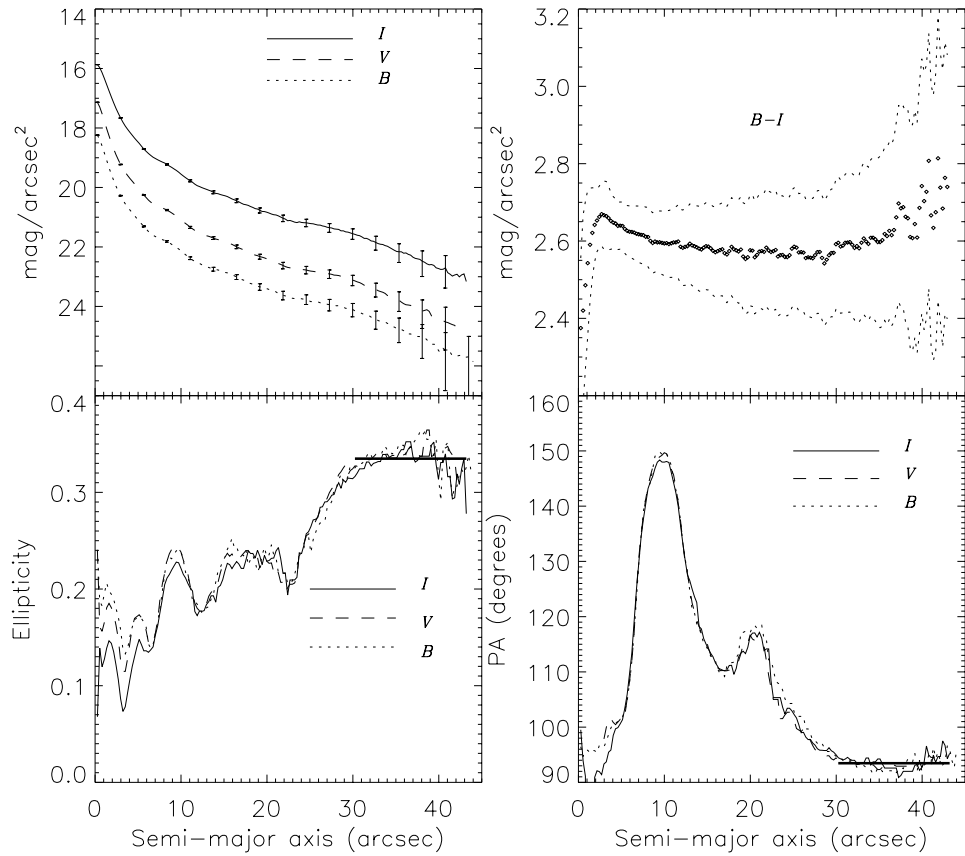


Figure 2. Surface brightness, ellipticity, position angle and $B - I$ colour radial profiles of ESO 139-G009. Continuous, dashed and dotted lines refer to I -, V - and B -band data, respectively. The thick lines represent the fits to the I -band ellipticity and PA of the galaxy in the disc region.

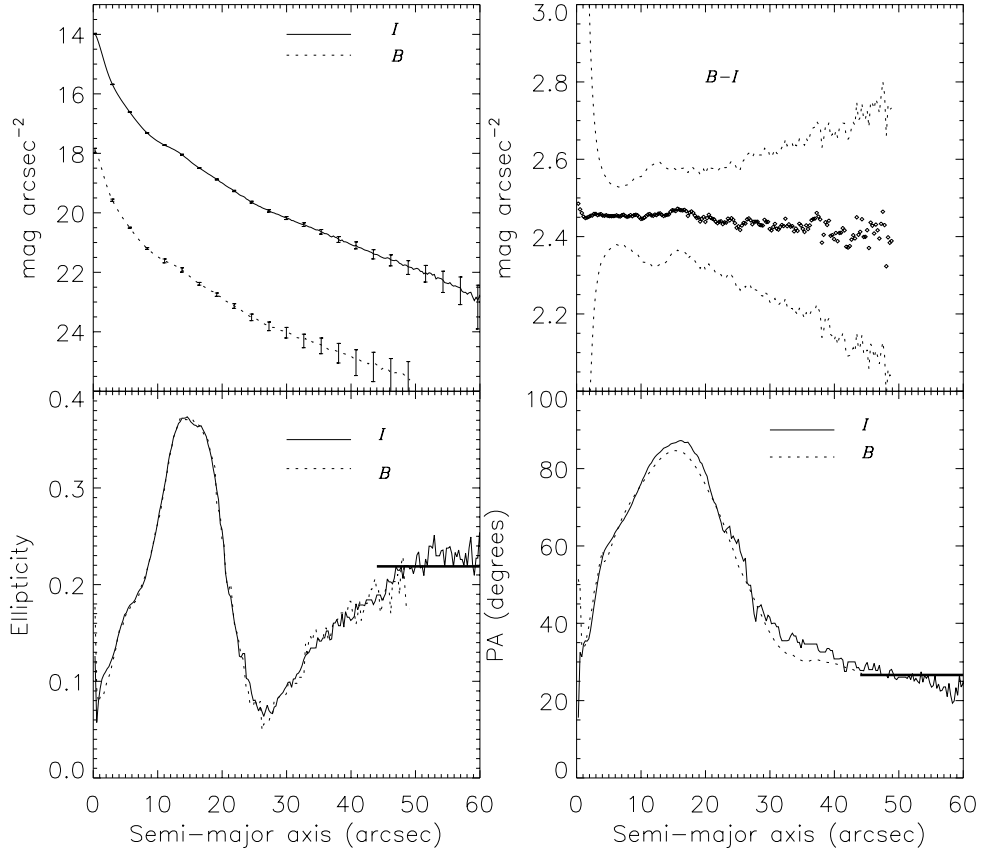


Figure 3. As in Fig. 2 but for IC 874.

studied in this paper. Because patchy obscuration can cause variations of ellipse centres, we conclude that there is no evidence for such obscuration in our sample, as we also verified from colour maps and $B - I$ colour profiles, where possible. The final ellipse fits were carried out at fixed ellipse centres. In Figs 2–6, we show the resulting surface brightness, $B - I$ colour, ellipticity and position angle profiles of the galaxies. The inclination and position angle of the galaxies were determined by averaging the outer isophotes, as shown in Fig. 1. The values obtained are reported in Table 3. The inclinations obtained for the galaxies are, within the errors, consistent with the values reported in the literature. The position angle has larger differences, the largest being $\Delta\text{PA} = 99^\circ$ in the case of NGC 1308. We speculate that the Lyon–Meudon Extragalactic data base (LEDA) value of the position angle for this galaxy is contaminated by the bright star to its east. In measuring the photometrical parameters of this galaxy, we masked out the whole eastern part, to minimize the contamination from this star. In the case of NGC 3412, it is possible to compare our values of i and PA with those obtained by Kent (1984), who found $i = 56.6^\circ$ and $\text{PA} = 151.6^\circ$. These data are in very good agreement with our measurements, as given in Table 3.

Using the ellipse fits, we measured the angle, ψ_{bar} , between the bar's major axis and the line of nodes in the deprojected plane of the disc. The values of this parameter are reported in Table 3.

4.2 Semimajor axis length of a bar

Determining the length of a bar is not entirely trivial. This is particularly true in early-type galaxies, for which there is usually no obvious spiral structure or star formation beyond the bar marking its end, so

that the luminosity distribution of the bar gradually melds into that of the disc. The presence of a large bulge may complicate further the measurement of a_B . Fourier decomposition of the galaxy light (Ohta, Masaru & Wakamatsu 1990; Aguerri et al. 2000), identification of a change in the slope of the surface-brightness profile along the bar's major axis (Chapelon, Contini & Davoust 1999), visual inspection of galaxy images (Martin 1995), location of min/max in the ellipticity profile (Wozniak et al. 1995), and modelling the structural components contributing to the galaxy surface brightness (Prieto et al. 2001) are among the several methods which have been proposed for measuring a_B . We have used three of these, yielding four estimates of a_B ($a_{B,1}$ to $a_{B,4}$). The mean of these is our best estimate of a_B and we use the largest deviations from the mean for the error estimates. The values obtained are given in Table 4. The three methods are the following:

(i) *Fourier amplitudes.* Because a bar represents a bisymmetric departure from axisymmetry, a Fourier decomposition is a natural way to measure a_B . The method of Aguerri et al. (2000) is based on the ratios of the intensities in the bar and the interbar region. The azimuthal surface-brightness profile of the deprojected galaxies is decomposed in a Fourier series. The bar intensity, I_b , then is defined as: $I_b = I_0 + I_2 + I_4 + I_6$ (where I_0 , I_2 , I_4 and I_6 are the $m = 0, 2, 4$ and 6 terms of the Fourier decomposition, respectively). The interbar intensity is defined as: $I_{ib} = I_0 - I_2 + I_4 - I_6$. The bar region is defined as the region where $I_b/I_{ib} > 0.5[\max(I_b/I_{ib}) - \min(I_b/I_{ib})] + \min(I_b/I_{ib})$; thus the semimajor axis of the bar is identified as the outer radius

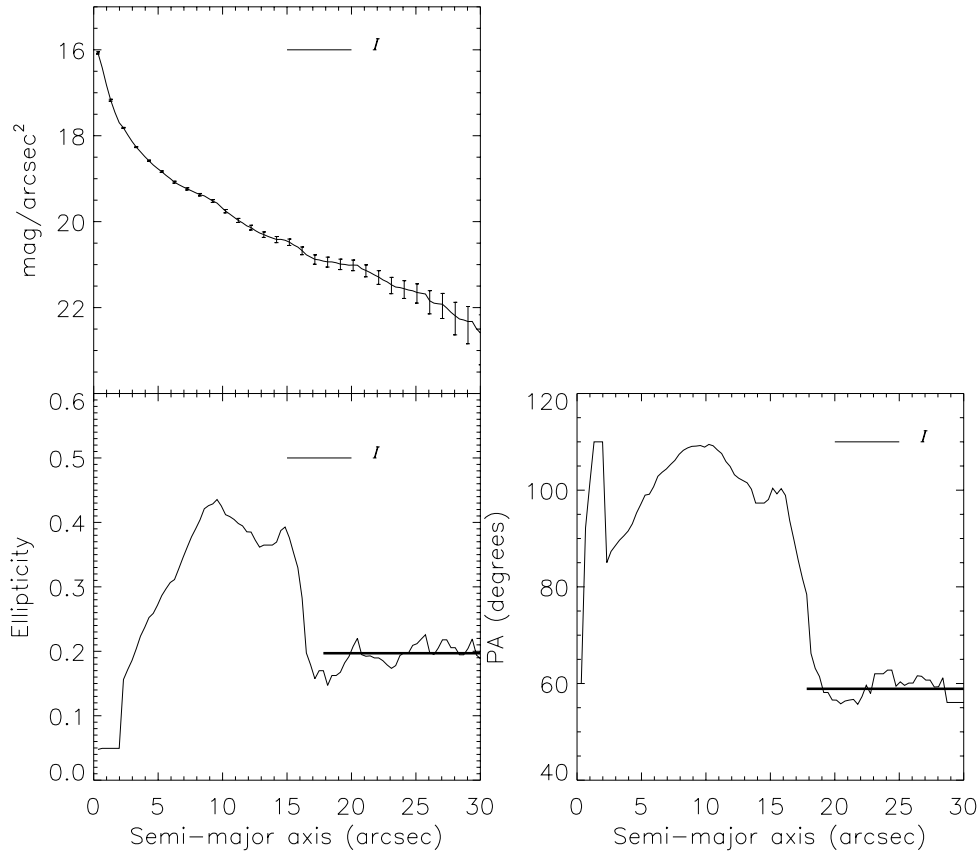


Figure 4. As in Fig. 2 but for NGC 1308. Only I -band data are available for this galaxy and therefore no $B - I$ colour radial profile is provided.

at which $I_b/I_{ib} = 0.5[\max(I_b/I_{ib}) - \min(I_b/I_{ib})] + \min(I_b/I_{ib})$. Athanassoula & Misiriotis (2002) applied this method to the analytic models of Athanassoula (1992) (for which a_B are known exactly) and found an accuracy of better than 8 per cent. In practical applications to early-type galaxies, adjustment for the presence of a massive bulge, which in deprojection may result in a higher peak in I_b/I_{ib} than that due to the bar, may be required (e.g. Paper I). The values listed as $a_{B,1}$ in Table 4 are those which were obtained using this method. Fig. 7 shows relative amplitudes of the $m = 2, 4, 6$ Fourier components and the bar/interbar intensity ratio of the galaxies.

(ii) *Fourier and ellipse phases.* In their analysis of N -body models, DeBattista & Sellwood (2000) also made use of a Fourier decomposition of the surface density. Here we adopt their $m = 2$ (deprojected) phase method for $a_{B,2}$, namely that a bar can extend only as far out as the phase of the $m = 2$ moment is constant (within the errors, which here must include uncertainties in PA and i). In N -body simulations, secondary structures, such as rings or spirals, sometimes lead to an overestimate of the semimajor axis. However, our early-type galaxies were selected to be free of spirals and rings. A related, but not equivalent, method uses the phases of the ellipse fits, which then gives us an estimate of $a_{B,3}$ in Table 4. In Fig. 7, we plot the phases of the Fourier $m = 2$ moments and of the ellipses, showing $a_{B,2}$ and $a_{B,3}$.

(iii) *Decomposition of surface-brightness profiles.* The surface-brightness profiles of galaxies can be decomposed into a number of structural components, each of which may be described by some

simple analytic model. Barred galaxy models are complicated by their non-axisymmetric nature; a method for such decompositions has been developed by Prieto et al. (2001), which we have used here. We have assumed four different components: bulge, disc, bar and lens. The bulge luminosity was modelled with a Sérsic's law (Sérsic 1968), while the disc was modelled by an exponential profile (Freeman 1970). Two profile types for the bars were used: elliptical (Freeman 1966) and flat (Prieto et al. 1997). The best fit for NGC 3412 was obtained with an elliptical bar; for the other galaxies, we used flat bars.

The lenses were characterized by a smooth luminosity gradient with a very sharp cut-off (Duval & Athanassoula 1983). The model of NGC 1308 did not need to include a lens; for all the other galaxies, the fit was improved by including a lens.

In all, 10 free parameters needed to be fitted: the central surface brightness and the scalelength of the disc, the effective surface brightness, the effective radius, and the Sérsic index of the bulge, the central surface brightness, the semimajor and the semiminor axes of the bar, the central surface brightness and the scale radius of the lens. The fits were performed on the major and minor axes of the bar, after deprojecting the image by means of a flux-conserving stretch along the minor axis of the disc.

We used an interactive, iterative method, described in Prieto et al. (2001) to obtain initial estimates of all the parameters. Then, these estimates of the parameters were used as input parameters in an automatic fitting routine using a Levenberg–Marquardt non-linear fitting algorithm (Press et al. 1992). Fig. 7 shows the best fit of the

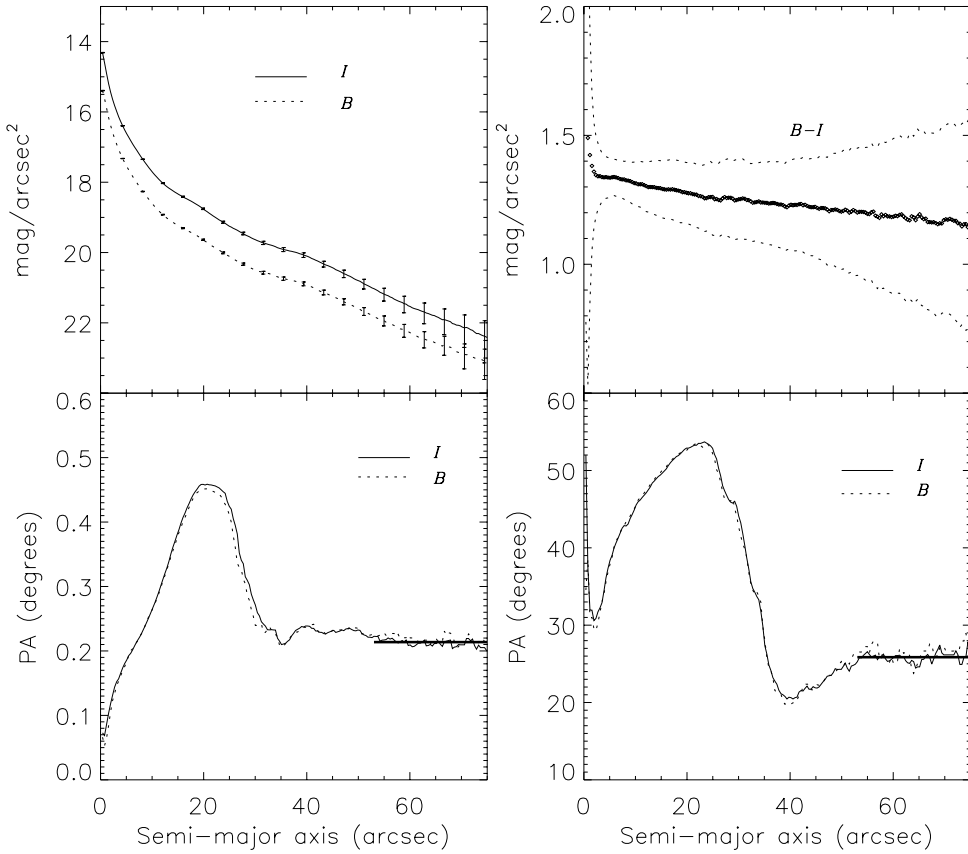


Figure 5. As in Fig. 2 but for NGC 1440.

surface-brightness profiles along the major axis of the bar for the galaxies of our sample. Table 4 also includes the semimajor axis of the bar measured with this method ($a_{B,4}$).

5 LONG-SLIT SPECTROSCOPY

The spectroscopic observations of ESO 139-G009, IC 874, NGC 1308 and NGC 1440 were carried out with the NTT at ESO in La Silla in 2001 May and November. The NTT mounted EMMI in red medium-dispersion spectroscopic (REMD) mode, using the grating No 6 with 1200 grooves mm⁻¹ in first order with a 1.0 arcsec \times 5.5 arcmin slit. The detector was the No 36 Tektronix TK2048 EB CCD with 2048 \times 2048 pixels of 24 \times 24 μm^2 . It yielded a wavelength coverage between about 4840 and 5490 Å with a reciprocal dispersion of 0.320 Å pixel⁻¹. The instrumental resolution was 1.19 Å (FWHM) corresponding to $\sigma_{\text{inst}} \approx 30 \text{ km s}^{-1}$ at 5170 Å. The spatial scale was 0.270 arcsec pixel⁻¹.

We observed NGC 3412 with the 3.6-m Telescopio Nazionale Galileo (TNG) at the ORM in La Palma in 2001 February. The TNG was equipped with the Low-Resolution Spectrograph (DOLORES); we used the HR-V grism No 6 with 600 grooves mm⁻¹ in combination with the 0.7 arcsec \times 8.1 arcmin slit and the Loral CCD with 2048 \times 2048 pixels of 15 \times 15 μm^2 . The wavelength range between about 4700 and 6840 Å was covered with a reciprocal dispersion of 1.055 Å pixel⁻¹. The instrumental resolution (obtained by measuring the width of emission lines of a comparison spectrum after the wavelength calibration) was 3.10 Å (FWHM). This corresponds to an instrumental dispersion of $\sigma_{\text{inst}} \approx 80 \text{ km s}^{-1}$ at 5170 Å. The spatial scale along the slit was 0.275 arcsec pixel⁻¹.

For each galaxy, we took a spectrum with the slit along the major axis, as well as two or more offset spectra with the slit parallel to the major axis on each side of the centre. The major axis position angles were chosen according to the values obtained from the surface photometry, as described in Section 4.1 and listed in Table 3. The location of the offset spectra was chosen, using the photometry, to give large χ^2 (and therefore large \mathcal{V}) and high signal-to-noise ratio (S/N). The integration time of the galaxy spectra was split into exposures of 2700/3600 s to deal with cosmic rays. A log of the observations is given in Table 5. In each observing run we obtained spectra of 12 giant stars with spectral type ranging from late-G to early-K, selected from Faber et al. (1985), to use as templates in measuring stellar kinematics. Arc lamp spectra were taken before and/or after every object exposure to allow an accurate wavelength calibration. The range of the seeing FWHM during the observing runs was 0.7–1.6 arcsec in 2001 February (as measured by fitting a two-dimensional Gaussian to the TNG guide star), 0.5–2.2 arcsec in 2001 May, and 0.5–1.5 arcsec in 2001 November (as measured by the ESO Differential Image Motion Monitor).

All the spectra were bias subtracted, flat-field corrected, cleaned of cosmic rays, corrected for bad pixels and columns, and wavelength calibrated using standard MIDAS² routines as in Paper I. We checked that the wavelength rebinning was done properly by measuring the difference between the measured and predicted wavelengths (Osterbrock et al. 1996) for the brightest night-sky emission lines in the observed spectral ranges. The resulting accuracy in the wavelength calibration is better than 2 km s⁻¹.

² MIDAS is developed and maintained by the European Southern Observatory.

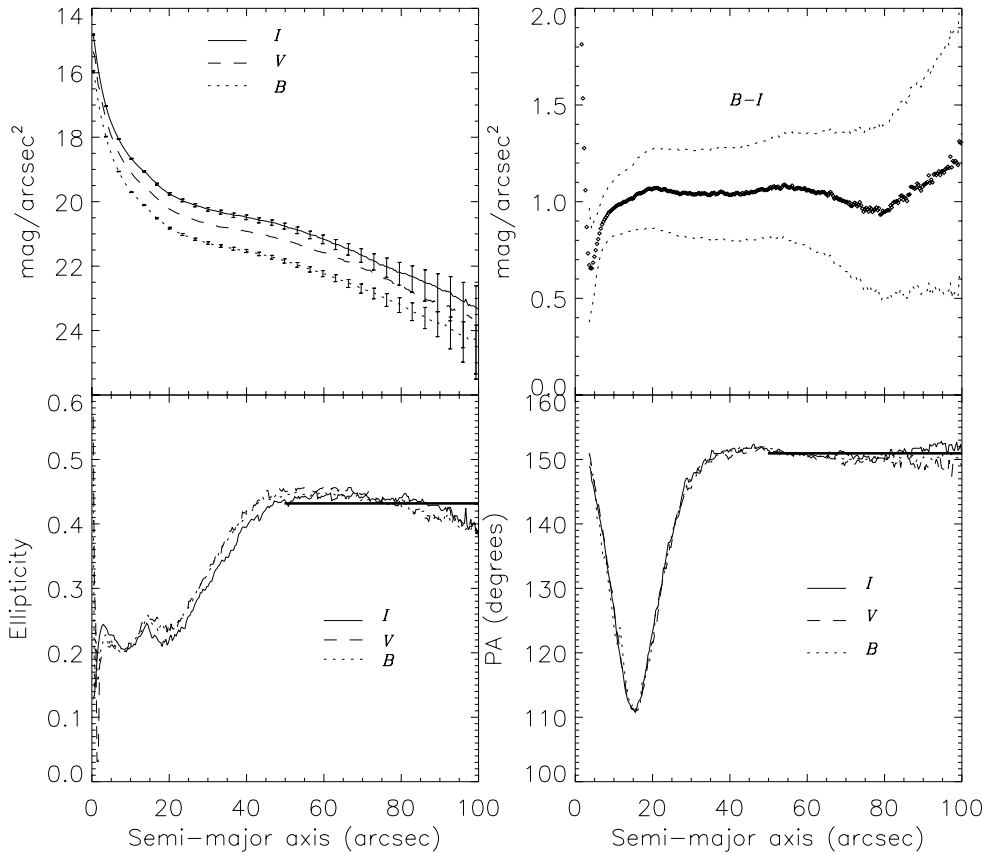


Figure 6. As in Fig. 2 but for NGC 3412.

Table 3. Inclination, disc position angle, and intrinsic bar angle relative to the line-of-nodes of the sample galaxies.

Galaxy	i ($^{\circ}$)	PA _{disc} ($^{\circ}$)	ψ_{bar} ($^{\circ}$)
ESO 139-G009	46.2 ± 1.5	93.5 ± 1.0	77 ± 1
IC 874	38.7 ± 1.8	26.6 ± 2.7	70 ± 3
NGC 1308	35.9 ± 2.6	58.9 ± 4.1	60 ± 1
NGC 1440	37.8 ± 0.9	25.9 ± 0.6	40 ± 1
NGC 3412	55.3 ± 2.1	151.0 ± 0.9	84 ± 2

Table 4. Bar semimajor axis of the galaxies.

Galaxy	$a_{B,1}$ (arcsec)	$a_{B,2}$ (arcsec)	$a_{B,3}$ (arcsec)	$a_{B,4}$ (arcsec)	$\langle a_B \rangle$ (arcsec)
ESO 139-G009	23.4	14.0	16.1	14.4	$17.0^{+6.4}_{-3.0}$
IC 874	18.7	21.0	25.0	15.0	$19.9^{+5.1}_{-4.9}$
NGC 1308	13.2	9.0	13.2	14.2	$12.4^{+1.8}_{-3.4}$
NGC 1440	23.2	24.6	30.5	19.2	$24.4^{+6.1}_{-5.2}$
NGC 3412	28.2	30.0	32.2	34.0	$31.1^{+2.9}_{-2.9}$

The spectra taken along the same axis for the same galaxy were co-added using the centre of the stellar continuum as a reference. The contribution of the sky was determined from the outermost ~ 30 arcsec at the two edges of the resulting spectra, where the galaxy light was negligible, and then subtracted, giving a sky subtraction

better than 1 per cent. A one-dimensional sky-subtracted spectrum was obtained for each kinematical template star.

6 BAR AND DISC KINEMATICS

6.1 Stellar kinematics

We measured the stellar kinematics from the galaxy absorption features present in the wavelength range centred on the Mg line triplet ($\lambda\lambda 5164, 5173, 5184 \text{ \AA}$, see Table 7) using the Fourier Correlation Quotient method (Bender 1990; Bender, Saglia & Gerhard 1994), as done in Paper I. We adopted HR 6817 (K1 III) as the kinematical template to measure the stellar kinematics of NGC 3412, HR 7429 (K3 III) for the kinematics of ESO 139-G009 and IC 874, and HR 3145 (K2 III) for the kinematics of NGC 1308 and 1440.

The values of line-of-sight velocity v , and velocity dispersion σ measured along the different slits for each sample galaxy are given in Table 6.

6.2 Pattern speed measurement

We measured the bar pattern speed for each sample galaxy by applying the TW method, as done in Paper I.

To compute the mean position of stars, \mathcal{X} , along the slits, we generally extracted profiles from I - and V -band surface photometry along the positions of the slits. In the case of NGC 1440, because of the radial colour gradient, we preferred to use the intensity from the slit spectra themselves, although they are somewhat noisier. For the remaining galaxies, the I -band profiles match very well the profiles

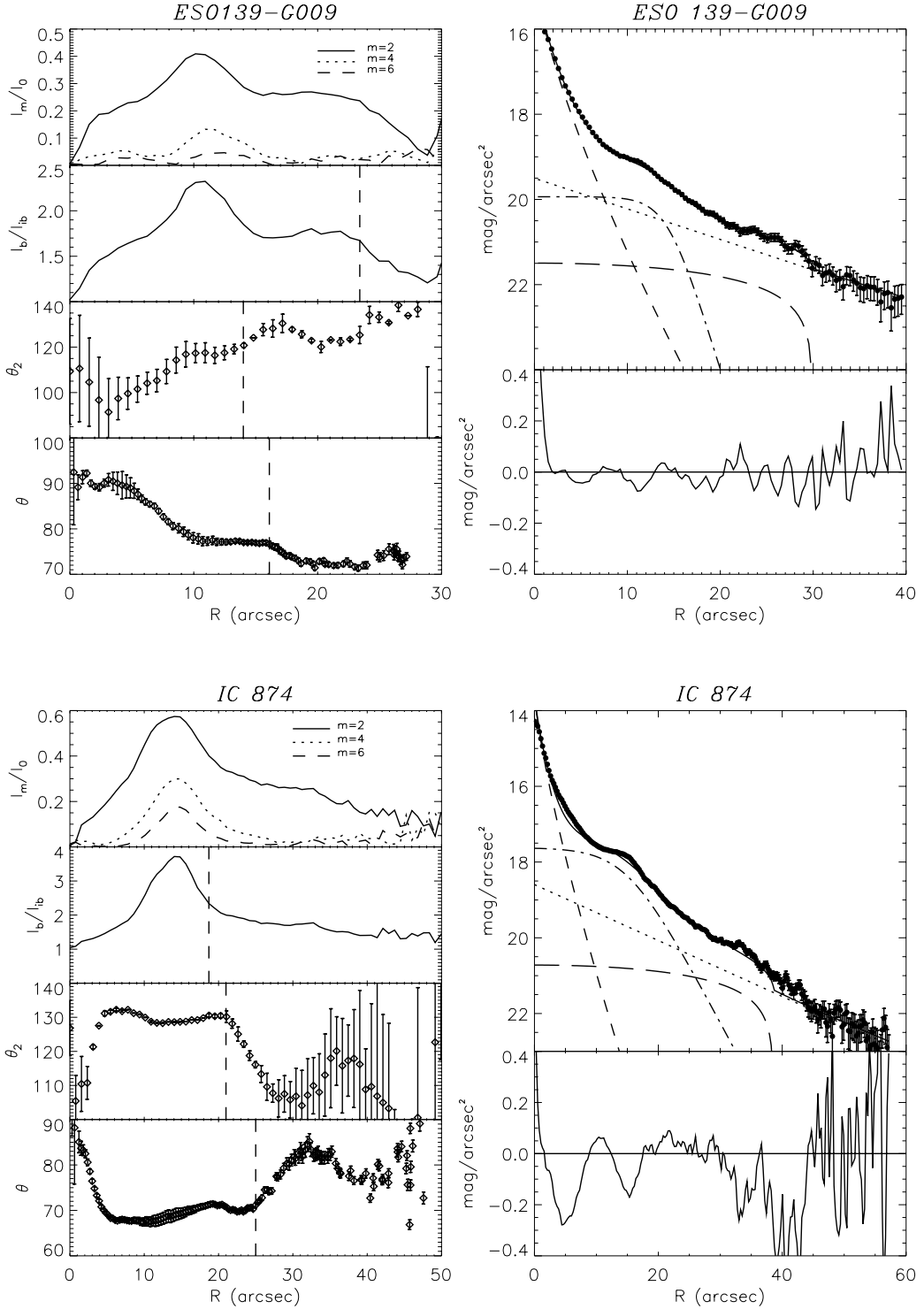


Figure 7. Bar semimajor axis length of the sample galaxies. Left panels (from top to bottom): Relative amplitudes of the $m = 2, 4, 6$ Fourier components, bar/interbar intensity ratio, phase angle of the $m = 2$ Fourier component, and position angle of the deprojected isophotal ellipses. The dashed vertical lines show the bar length ($a_{B,1}, a_{B,2}$ and $a_{B,3}$ of Table 4). Right panels (from top to bottom): Decomposition of the radial surface-brightness profiles in I -band along the major axis of the bar, and residuals of the fit. The adopted structural components are bulge (dashed line), disc (dotted line), bar (dash-dotted line) and lens (long-dashed line). The continuous line represents the total model.

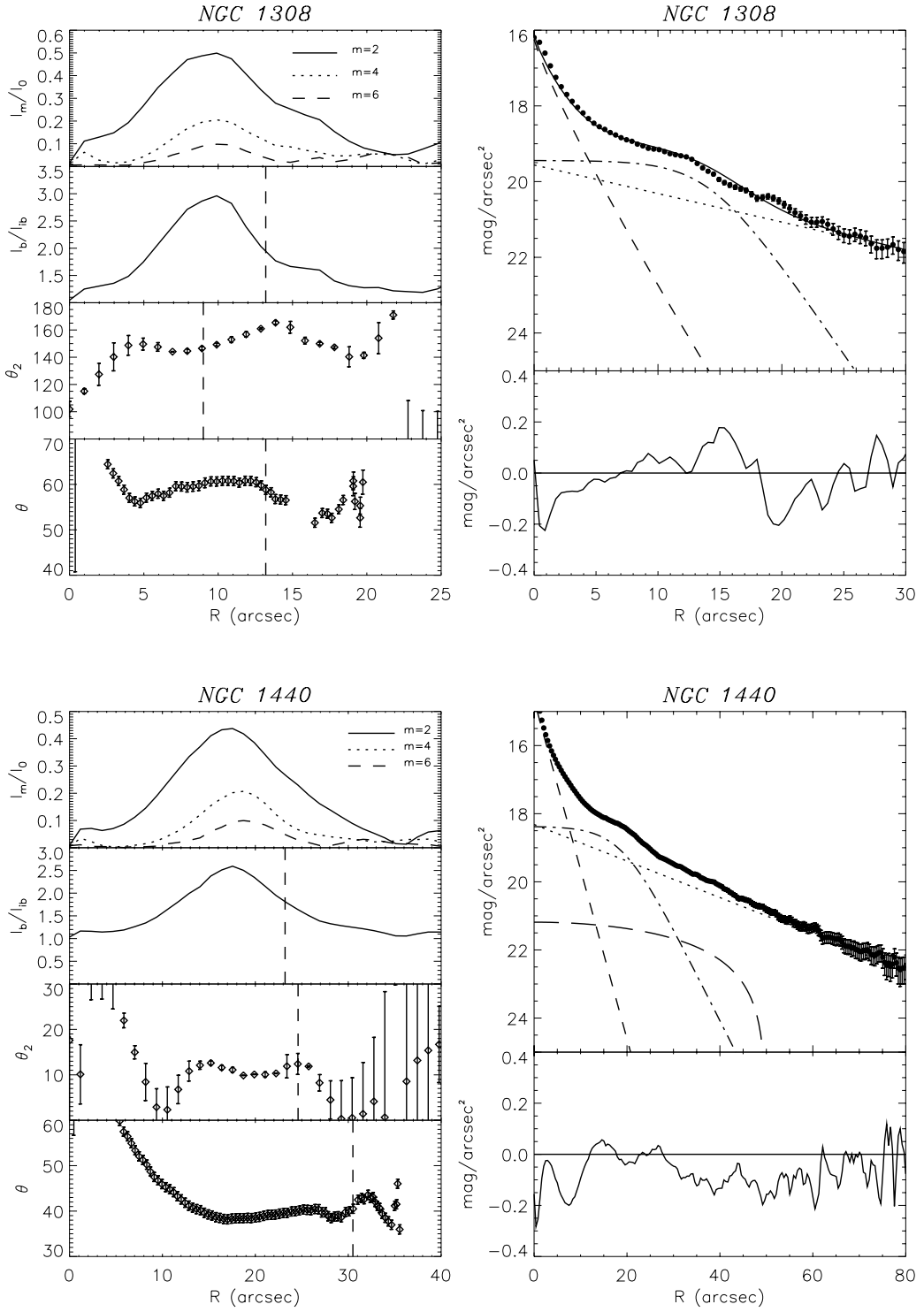


Figure 7 – continued

obtained by collapsing the spectra along the wavelength direction, confirming that the slits were placed as intended. We used the broadband profiles to compute \mathcal{X} because these are less noisy than the spectral profiles, particularly at large radii. We computed the value of \mathcal{X} at each slit position by Monte Carlo simulation, with photon, readout and sky noise to compute the errors. Formally, the integrals in the TW equation are over $-\infty \leq X \leq \infty$, but can be limited to $-X_{\max} \leq X \leq X_{\max}$ if X_{\max} has reached the axisymmetric part of

the disc; still larger values of X_{\max} add noise only. The \mathcal{X} values thus obtained are given in Table 7.

To measure the luminosity-weighted line-of-sight stellar velocity, \mathcal{V} , for each slit position, we collapsed each two-dimensional spectrum along its spatial direction to obtain a one-dimensional spectrum. The resulting spectra have been analysed with the FCQ method using the same template star adopted in Section 6.1 to derive the stellar kinematics of the galaxy; \mathcal{V} is then the radial velocity

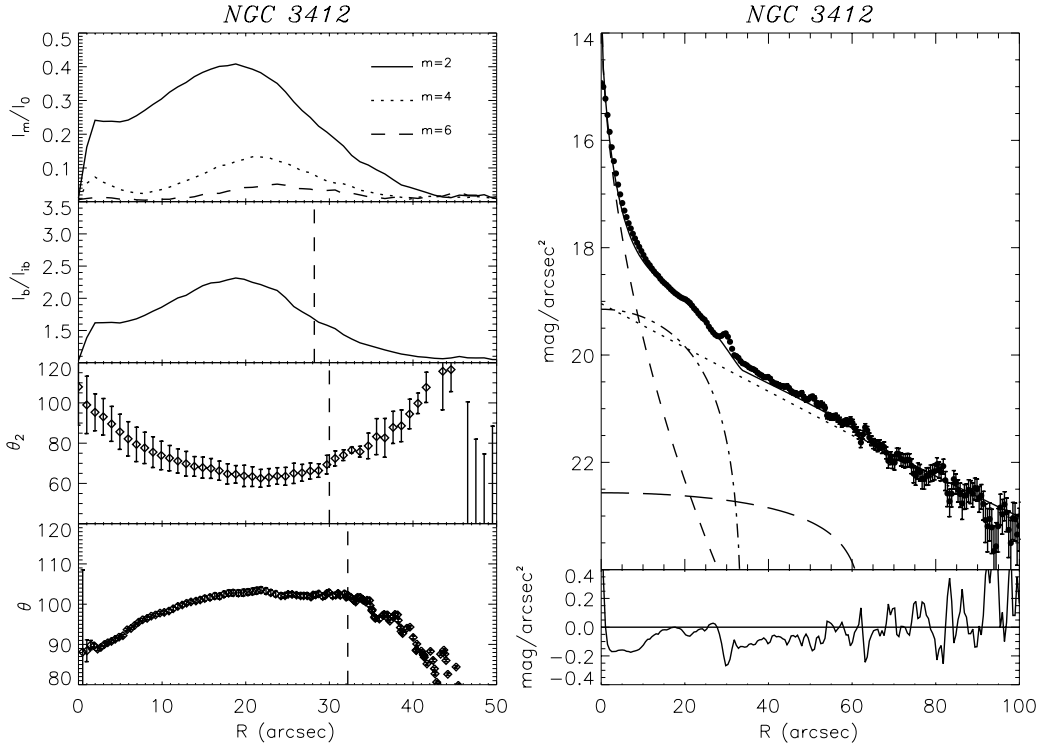


Figure 7 – continued

Table 5. Log of the spectroscopic observations. (N – north, S – south, E – east, W – west.)

Galaxy	Date	Slit	Exp. Time (s)
ESO 139-G009	2001 May 24	10 arcsec N	7200
	2001 May 23	major axis	5400
	2001 May 23	8 arcsec S	7200
IC 874	2001 May 23	10 arcsec E	10800
	2001 May 22	major axis	5400
	2001 May 24	10 arcsec W	10800
NGC 1308	2001 Nov 15	5 arcsec E	10800
	2001 Nov 17	major axis	5400
	2001 Nov 16	5 arcsec W	10800
NGC 1440	2001 Nov 17	9 arcsec E	7200
	2001 Nov 15	6 arcsec E	5400
	2001 Nov 15	major axis	5400
	2001 Nov 16	6 arcsec W	5400
	2001 Nov 17	11 arcsec W	7200
NGC 3412	2001 Feb 01	10 arcsec E	7200
	2001 Feb 02	major axis	7200
	2001 Feb 01	10 arcsec W	7200
	2001 Feb 02	15 arcsec W	7200

derived from the LOSVD of the one-dimensional spectra. For each slit position, the uncertainty on \mathcal{V} was estimated by means of Monte Carlo simulations, as for v in measuring the stellar kinematics.

Table 7 gives the \mathcal{V} values we derived along each slit and the adopted wavelength (always including the Mg triplet) and radial ranges (limited by the noise, and after removing the contribution of foreground stars by linear interpolation).

For each galaxy, we derived $\Omega_p \sin i$ by fitting a straight line to the values (\mathcal{X} and \mathcal{V}) obtained from the available slit positions

(Fig. 9). Finally the value of Ω_p (Table 8) was derived from the adopted galaxy inclination, as given in Table 3.

6.3 Systemic and mean streaming velocities

To measure the systemic velocity of the galaxies, we fitted interpolating splines to the measured velocities and fitted ‘tilted rings’, of fixed i and PA (as obtained from the photometry), to the inner parts of the galaxies. In the case of NGC 1308, our data were not of sufficient S/N to permit such fits, in which case we used \mathcal{V} on the major axis; for the other four galaxies, comparison of Tables 7 and 8 shows that the major axis \mathcal{V} is a very good approximation to V_{sys} . In Table 8, we compare our measurements of V_{sys} with those in RC3. In all cases we find excellent agreement.

Once V_{sys} is measured, we obtain the stellar mean streaming velocities, V_* , by subtracting V_{sys} , then folding about the origin the major-axis data. Fig. 8 shows that our folded spectra have no substantial asymmetries on the two sides.

6.4 Asymmetric drift correction

Measurement of Ω_p with the TW method requires no modelling. However, in the absence of gas velocities at large radii, measurement of \mathcal{R} requires some modelling to recover the rotation curve from the observed stellar streaming velocities. This asymmetric drift correction can be fairly large in early-type disc galaxies, where the velocity dispersions are large. We start from the asymmetric drift equation [e.g. Binney & Tremaine 1987, equations (4)–(33)]

$$V_c^2 - V_*^2 = -\sigma_R^2 \left[\frac{\partial \ln \rho}{\partial \ln R} + \frac{\partial \ln \sigma_R^2}{\partial \ln R} + \left(1 - \frac{\sigma_\phi^2}{\sigma_R^2} \right) \right], \quad (1)$$

where V_c is the circular velocity, ρ is the disc’s volume density, and σ_ϕ and σ_R are the tangential and radial velocity dispersions in

Table 6. Stellar kinematics of the sample galaxies.

<i>r</i> (arcsec)	<i>v</i> (km s ⁻¹)	σ (km s ⁻¹)
ESO 139-G009 – 10 arcsec N		
-18.78	5262.1 ± 23.9	90.3 ± 14.1
-3.68	5321.0 ± 8.4	80.0 ± 9.0
7.54	5454.0 ± 9.3	88.9 ± 9.1
21.48	5541.2 ± 20.7	72.6 ± 16.2
ESO 139-G009 – major axis		
-24.33	5174.2 ± 8.4	64.6 ± 8.2
-7.87	5221.3 ± 9.2	125.5 ± 8.8
-3.22	5285.5 ± 15.6	168.4 ± 30.8
-1.69	5316.1 ± 14.0	180.5 ± 31.6
-0.93	5339.8 ± 7.0	186.1 ± 5.7
-0.39	5355.3 ± 5.9	202.4 ± 4.5
0.14	5382.3 ± 5.3	190.0 ± 4.1
0.67	5412.7 ± 5.5	188.1 ± 4.1
1.32	5429.6 ± 6.4	171.6 ± 5.4
2.45	5460.2 ± 18.0	173.3 ± 25.6
5.24	5505.2 ± 7.4	143.6 ± 6.3
18.53	5572.6 ± 8.3	65.3 ± 7.9
ESO 139-G009 – 8 arcsec S		
-19.38	5217.0 ± 15.6	74.9 ± 18.4
-5.66	5279.9 ± 7.7	83.6 ± 7.4
1.05	5391.0 ± 10.2	102.0 ± 10.6
14.92	5473.6 ± 25.4	132.4 ± 23.6
IC 874 – 10 arcsec E		
-33.45	2247.4 ± 12.4	89.1 ± 19.0
-16.40	2239.7 ± 8.2	71.4 ± 8.3
-7.69	2272.4 ± 4.4	68.0 ± 4.3
-3.89	2293.8 ± 4.4	67.3 ± 3.9
1.57	2345.2 ± 6.8	79.4 ± 6.1
15.11	2376.9 ± 8.8	54.0 ± 6.7
IC 874 – major axis		
-28.36	2214.2 ± 9.1	43.3 ± 13.9
-11.17	2213.6 ± 8.3	86.0 ± 10.8
-6.73	2238.7 ± 5.9	96.2 ± 7.0
-4.72	2252.2 ± 3.9	93.8 ± 4.7
-3.29	2272.8 ± 3.6	99.6 ± 4.4
-2.35	2267.4 ± 3.4	98.0 ± 4.2
-1.69	2262.6 ± 3.1	96.6 ± 3.9
-1.15	2276.7 ± 2.3	101.4 ± 3.0
-0.76	2287.6 ± 2.4	101.1 ± 2.9
-0.49	2287.4 ± 2.5	106.2 ± 3.2
-0.22	2299.4 ± 2.0	97.4 ± 2.5
0.05	2312.4 ± 2.1	100.7 ± 2.8
0.32	2317.2 ± 2.1	98.5 ± 2.6
0.59	2329.3 ± 2.4	104.6 ± 3.1
0.86	2340.2 ± 2.9	108.0 ± 3.9
1.25	2353.0 ± 2.2	95.9 ± 2.9
1.79	2356.2 ± 3.0	106.2 ± 4.1
2.45	2355.7 ± 3.2	103.8 ± 4.1
3.51	2351.7 ± 3.2	94.9 ± 3.6
5.20	2356.5 ± 3.5	80.0 ± 3.1
7.03	2385.7 ± 8.1	95.3 ± 9.5
13.29	2411.7 ± 7.4	71.1 ± 6.1
32.84	2397.4 ± 8.0	63.6 ± 14.6
IC 874 – 10 arcsec W		
-30.18	2243.4 ± 17.0	79.7 ± 12.5
-12.54	2266.0 ± 6.8	65.1 ± 6.2
-1.34	2296.5 ± 5.6	67.1 ± 4.9
3.54	2335.1 ± 4.4	69.4 ± 4.0
7.23	2357.5 ± 4.2	64.2 ± 4.1
15.78	2373.3 ± 7.8	74.7 ± 7.0

Table 6 – continued

<i>r</i> (arcsec)	<i>v</i> (km s ⁻¹)	σ (km s ⁻¹)
NGC 1308 – 5 arcsec E		
35.47	2395.4 ± 13.0	53.0 ± 11.7
-19.45	6176.9 ± 20.0	142.7 ± 27.1
-8.25	6257.5 ± 10.0	125.6 ± 9.2
-3.70	6339.2 ± 8.6	157.0 ± 9.1
-0.54	6424.0 ± 7.7	140.0 ± 10.8
5.79	6494.4 ± 9.3	87.6 ± 9.2
14.97	6472.7 ± 17.8	69.4 ± 22.4
NGC 1308 – major axis		
-15.22	6131.4 ± 12.6	76.9 ± 18.7
-3.69	6244.0 ± 10.2	188.7 ± 15.8
-1.28	6277.2 ± 8.1	208.7 ± 10.5
-0.28	6321.6 ± 7.2	218.9 ± 10.9
0.48	6368.7 ± 8.6	231.8 ± 11.7
1.60	6392.5 ± 9.5	222.5 ± 14.1
6.25	6453.5 ± 13.3	158.4 ± 14.8
21.31	6505.5 ± 19.7	63.4 ± 19.0
NGC 1308 – 5 arcsec W		
-12.88	6124.4 ± 11.3	67.1 ± 13.5
-2.74	6173.8 ± 9.5	122.8 ± 10.2
1.57	6277.5 ± 9.2	148.0 ± 12.6
4.39	6330.4 ± 8.1	141.0 ± 10.9
8.92	6403.7 ± 12.7	164.1 ± 17.2
19.76	6481.6 ± 13.7	84.2 ± 10.5
NGC 1440 – 9 arcsec E		
-28.77	1471.1 ± 6.5	80.6 ± 7.0
-12.03	1503.8 ± 5.8	109.0 ± 5.7
-1.21	1586.3 ± 4.6	125.2 ± 3.4
5.53	1631.6 ± 4.5	118.3 ± 3.7
12.49	1680.8 ± 3.3	95.9 ± 3.6
23.74	1732.9 ± 3.7	70.3 ± 5.0
38.51	1764.4 ± 6.6	62.0 ± 9.2
NGC 1440 – 6 arcsec E		
-39.57	1443.5 ± 8.3	76.6 ± 9.5
-21.32	1458.5 ± 5.2	90.4 ± 5.7
-8.82	1528.2 ± 4.8	136.8 ± 3.8
-4.42	1558.9 ± 4.4	142.6 ± 3.4
-1.94	1564.0 ± 4.5	149.5 ± 3.9
0.06	1596.3 ± 4.5	152.8 ± 3.6
1.92	1607.7 ± 4.3	161.9 ± 3.7
3.92	1625.2 ± 4.5	153.1 ± 4.0
6.32	1636.3 ± 4.2	134.3 ± 3.3
9.60	1659.9 ± 4.4	132.9 ± 3.6
15.16	1686.4 ± 5.2	119.3 ± 4.6
30.70	1755.2 ± 4.3	71.1 ± 5.8
NGC 1440 – major axis		
-40.26	1444.5 ± 7.4	40.4 ± 7.9
-23.27	1455.5 ± 4.6	74.8 ± 6.0
-12.34	1509.3 ± 5.8	121.0 ± 4.6
-8.05	1544.7 ± 5.4	140.4 ± 4.3
-5.70	1541.1 ± 5.2	159.4 ± 4.3
-4.10	1537.0 ± 6.0	171.9 ± 5.3
-2.90	1542.6 ± 5.4	182.0 ± 4.9
-1.96	1547.9 ± 5.7	195.5 ± 5.6
-1.30	1547.8 ± 5.9	191.7 ± 6.0
-0.76	1567.3 ± 5.4	191.1 ± 5.3
-0.22	1592.4 ± 4.7	197.6 ± 4.9
0.31	1625.8 ± 4.4	192.6 ± 4.1
0.85	1646.0 ± 5.2	186.6 ± 5.2
1.38	1653.8 ± 5.6	181.5 ± 4.9
2.05	1664.0 ± 5.5	187.2 ± 5.0

Table 6 – continued

<i>r</i> (arcsec)	<i>v</i> (km s ⁻¹)	σ (km s ⁻¹)
2.98	1676.0 ± 5.5	179.7 ± 4.9
4.19	1667.9 ± 6.4	179.2 ± 5.8
5.90	1655.9 ± 5.9	162.5 ± 5.3
8.72	1673.0 ± 7.6	147.8 ± 6.2
15.18	1715.7 ± 7.5	123.3 ± 5.7
32.73	1748.6 ± 5.4	59.8 ± 6.5
NGC 1440 – 6 arcsec W		
-42.55	1463.1 ± 13.3	104.4 ± 13.4
-25.35	1458.2 ± 3.8	67.8 ± 4.8
-14.37	1498.4 ± 4.2	125.4 ± 3.4
-9.42	1545.8 ± 4.4	135.2 ± 3.4
-6.40	1568.3 ± 4.9	155.7 ± 4.2
-4.27	1580.3 ± 5.3	167.9 ± 4.6
-2.40	1595.6 ± 4.4	156.4 ± 3.7
-0.54	1615.8 ± 5.1	170.8 ± 4.4
1.46	1635.7 ± 5.0	164.6 ± 4.2
3.94	1643.5 ± 4.7	141.7 ± 3.6
8.52	1683.5 ± 6.5	137.0 ± 5.8
22.89	1744.0 ± 4.5	73.9 ± 6.6
41.65	1748.0 ± 9.4	85.0 ± 9.6
NGC 1440 – 11 arcsec W		
-36.82	1461.5 ± 7.5	75.1 ± 9.0
-19.80	1498.6 ± 4.5	86.2 ± 5.3
-11.21	1549.9 ± 5.8	118.5 ± 4.4
-3.37	1592.1 ± 7.1	137.4 ± 5.7
8.03	1688.1 ± 6.4	105.5 ± 6.7
28.29	1729.6 ± 7.1	71.9 ± 8.3
NGC 3412 – 10 arcsec E		
-67.31	701.8 ± 24.9	114.3 ± 35.1
-48.21	729.4 ± 12.6	91.4 ± 13.5
-34.56	727.8 ± 12.4	112.2 ± 14.4
-24.17	760.9 ± 9.2	93.2 ± 9.0
-15.93	761.9 ± 9.3	103.7 ± 9.8
-9.77	793.5 ± 8.6	105.9 ± 9.3
-5.15	816.4 ± 6.4	100.7 ± 6.5
-1.47	827.6 ± 7.5	109.1 ± 8.2
1.67	844.8 ± 6.7	101.7 ± 6.8
4.54	865.3 ± 6.5	105.4 ± 7.1
7.40	876.0 ± 6.9	93.0 ± 6.3
10.63	897.2 ± 8.3	97.9 ± 8.3
14.84	907.4 ± 7.3	85.4 ± 6.3
20.82	919.4 ± 10.3	108.9 ± 11.5
29.48	935.7 ± 14.0	108.6 ± 17.9
41.32	962.1 ± 18.8	132.3 ± 25.4
59.71	964.5 ± 16.9	97.4 ± 22.3
NGC 3412 – major axis		
-70.26	720.5 ± 33.0	82.9 ± 51.5
-52.52	751.3 ± 17.1	96.2 ± 20.9
-38.00	756.9 ± 13.3	100.7 ± 15.3
-27.50	759.4 ± 10.8	87.9 ± 10.8
-19.78	755.6 ± 10.3	98.4 ± 10.6
-14.24	777.7 ± 7.5	92.8 ± 6.7
-10.77	796.7 ± 7.4	105.9 ± 7.9
-8.47	810.5 ± 6.8	107.7 ± 7.5
-6.84	804.4 ± 6.9	110.4 ± 7.3
-5.61	808.9 ± 5.7	107.7 ± 6.0
-4.66	803.5 ± 5.2	106.5 ± 5.4
-3.98	815.6 ± 6.1	123.2 ± 7.3
-3.43	820.3 ± 5.9	123.8 ± 6.6
-2.88	826.9 ± 5.1	120.6 ± 5.8
-2.48	828.7 ± 6.9	124.1 ± 8.0

Table 6 – continued

<i>r</i> (arcsec)	<i>v</i> (km s ⁻¹)	σ (km s ⁻¹)
-2.20	826.5 ± 6.5	131.1 ± 7.7
-1.93	839.7 ± 6.7	127.0 ± 7.7
-1.65	835.3 ± 6.9	133.2 ± 8.3
-1.38	845.0 ± 5.9	124.4 ± 6.8
-1.10	845.8 ± 5.4	123.1 ± 6.2
-0.83	849.5 ± 5.2	118.9 ± 6.0
-0.55	850.8 ± 5.6	117.0 ± 6.2
-0.28	845.3 ± 5.5	114.2 ± 6.1
0.00	848.8 ± 5.2	109.6 ± 5.6
0.27	840.2 ± 6.1	111.4 ± 6.5
0.55	845.1 ± 5.2	117.1 ± 5.7
0.82	849.7 ± 6.6	124.5 ± 7.5
1.10	849.4 ± 5.7	115.4 ± 6.1
1.37	854.4 ± 6.8	127.9 ± 7.6
1.65	849.5 ± 7.0	123.6 ± 7.3
1.92	855.9 ± 7.9	139.6 ± 9.2
2.33	857.8 ± 5.3	121.7 ± 6.2
2.88	860.4 ± 5.8	129.7 ± 7.2
3.43	872.5 ± 6.3	129.1 ± 7.3
4.11	881.5 ± 6.1	128.6 ± 7.2
4.94	885.9 ± 7.2	114.6 ± 8.1
5.89	893.3 ± 6.5	105.4 ± 6.7
7.12	895.8 ± 6.2	99.0 ± 6.1
8.75	909.4 ± 8.4	102.2 ± 8.8
11.15	922.1 ± 8.3	101.3 ± 8.3
14.94	933.1 ± 9.3	101.8 ± 9.6
20.74	949.1 ± 11.5	99.5 ± 12.7
28.62	948.8 ± 13.1	95.5 ± 15.0
39.03	955.0 ± 13.4	81.5 ± 14.4
52.46	957.9 ± 16.3	92.8 ± 21.1
69.24	949.7 ± 33.3	72.6 ± 51.3
NGC 3412 – 10 arcsec W		
-57.08	717.2 ± 17.6	98.8 ± 20.4
-39.24	744.2 ± 11.7	89.0 ± 12.7
-27.61	765.3 ± 8.5	82.4 ± 6.9
-19.30	779.4 ± 7.3	86.5 ± 6.4
-13.62	801.1 ± 7.0	89.8 ± 6.3
-9.68	815.3 ± 5.6	78.4 ± 4.4
-6.71	831.0 ± 6.1	96.1 ± 5.9
-3.98	848.6 ± 6.7	103.0 ± 6.9
-1.25	860.7 ± 6.3	95.1 ± 6.1
1.62	873.5 ± 6.4	93.7 ± 6.0
4.87	882.8 ± 7.2	92.4 ± 6.6
8.92	902.7 ± 8.1	99.1 ± 8.4
14.56	938.0 ± 7.4	85.6 ± 6.0
22.24	944.8 ± 10.1	98.7 ± 10.9
32.26	957.8 ± 11.8	96.1 ± 13.8
45.31	978.9 ± 15.3	106.7 ± 19.5
63.88	955.0 ± 18.6	69.6 ± 27.0
NGC 3412 – 15 arcsec W		
-61.49	725.2 ± 29.0	108.3 ± 38.2
-39.65	741.8 ± 13.9	77.4 ± 15.5
-25.09	755.6 ± 9.9	95.9 ± 9.7
-14.98	800.7 ± 8.2	83.8 ± 7.2
-8.14	824.5 ± 6.9	80.9 ± 5.4
-2.65	840.0 ± 8.0	95.7 ± 7.9
3.32	866.8 ± 8.4	92.8 ± 8.1
10.81	910.3 ± 10.2	104.4 ± 10.9
20.71	923.8 ± 10.7	89.1 ± 10.9
33.33	945.6 ± 14.5	87.1 ± 17.0
52.54	952.0 ± 15.5	76.4 ± 18.6

Table 7. The values of \mathcal{V} and \mathcal{X} for each slit of our sample of galaxies.

Galaxy	Offset	\mathcal{X} (arcsec)	\mathcal{V} (km s $^{-1}$)	$ X _{\max}$ (arcsec)	$\lambda_{\min}, \lambda_{\max}$ (Å)
ESO 139-G009	10 arcsec N	$+1.07 \pm 0.03$	5406.4 ± 7.0	40	5014.1, 5486.2
	major axis	-0.12 ± 0.02	5375.0 ± 6.2	60	5014.1, 5486.2
	8 arcsec S	-1.62 ± 0.08	5366.0 ± 8.4	50	5014.1, 5486.2
IC 874	10 arcsec E	-1.86 ± 0.04	2305.6 ± 4.3	55	5039.2, 5486.2
	major axis	$+0.01 \pm 0.06$	2315.4 ± 1.4	80	5039.2, 5486.2
	10 arcsec W	$+2.07 \pm 0.06$	2323.1 ± 4.0	55	5039.2, 5486.2
NGC 1308	5 arcsec E	-1.51 ± 0.01	6358.1 ± 14.7	35	5115.3, 5431.7
	major axis	-0.01 ± 0.00	6328.7 ± 15.7	35	5115.3, 5431.7
	5 arcsec W	$+1.45 \pm 0.01$	6288.6 ± 18.7	35	5115.3, 5431.7
NGC 1440	9 arcsec E	-2.35 ± 0.10	1625.1 ± 5.7	50	5115.3, 5431.7
	6 arcsec E	-1.46 ± 0.10	1603.5 ± 3.5	50	5115.3, 5431.7
	major axis	$+0.25 \pm 0.10$	1599.8 ± 3.2	50	5115.3, 5431.7
	6 arcsec W	$+2.21 \pm 0.10$	1594.8 ± 3.9	50	5115.3, 5431.7
	11 arcsec W	$+4.47 \pm 0.10$	1581.2 ± 7.9	50	5115.3, 5431.7
NGC 3412	10 arcsec E	-1.46 ± 0.13	843.2 ± 1.8	80	4964.2, 5541.4
	major axis	-0.06 ± 0.03	849.1 ± 1.0	80	4964.2, 5541.4
	10 arcsec W	$+1.19 \pm 0.07$	852.3 ± 2.0	80	4964.2, 5541.4
	15 arcsec W	$+0.83 \pm 0.06$	853.5 ± 4.0	80	4964.2, 5541.4

Table 8. Disc and bar kinematics.

Galaxy	V_{sys} (km s $^{-1}$)	$V_{\text{sys,RC3}}$ (km s $^{-1}$)	$V_{\text{c,flat}}$ (km s $^{-1}$)	Ω_p (km s $^{-1}$ arcsec $^{-1}$)	D_L (arcsec)	\mathcal{R}
ESO 139-G009	5377 ± 6	5370 ± 60	314^{+14}_{-12}	21.4 ± 5.8	$14.7^{+5.2}_{-3.1}$	$0.8^{+0.3}_{-0.2}$
IC 874	2309 ± 4	2311 ± 36	187^{+14}_{-13}	7.0 ± 2.4	$26.9^{+13.1}_{-6.8}$	$1.4^{+0.7}_{-0.4}$
NGC 1308	6329 ± 16	6350 ± 42	347^{+21}_{-18}	39.7 ± 13.9	$8.9^{+4.5}_{-2.3}$	$0.8^{+0.4}_{-0.2}$
NGC 1440	1601 ± 2	1534 ± 66	283^{+11}_{-9}	7.4 ± 1.7	$38.3^{+10.7}_{-7.0}$	$1.6^{+0.5}_{-0.3}$
NGC 3412	850 ± 2	865 ± 27	205^{+18}_{-15}	4.4 ± 1.2	$46.9^{+17.3}_{-9.9}$	$1.5^{+0.6}_{-0.3}$

the cylindrical coordinates of the galaxy's intrinsic plane. We then make the following assumptions:

(i) We assume that the true rotation curve is flat at large radii. This is usually a very good approximation in high surface-brightness galaxies. Thus we only measure $V_{\text{c,flat}}$, the amplitude of the rotation curve. A flat rotation curve implies $\sigma_\phi^2/\sigma_R^2 = \frac{1}{2}$, which allows us to write, for the observed velocity dispersion on the major axis, $\sigma_{\text{obs}} = \sigma_\phi \sin i \sqrt{1 + 2\alpha^2 \cot^2 i}$, where $\alpha = \sigma_z/\sigma_R$. We use three values of α , 0.7, 0.85 and 1.0, which bracket a plausible range for this parameter in early-type disc galaxies extrapolating from the only three measured values in later-type systems (Dehnen & Binney 1998; Gerssen, Kuijken & Merrifield 1997, 2000). The variations in this parameter are included in our error estimate of $V_{\text{c,flat}}$.

(ii) We assume that σ_{obs} decreases exponentially with radius, with scalelength R_σ . We fit R_σ with the major-axis data, outside the bar region when the S/N permits; these fits are shown in Fig. 8.

(iii) We assume that the disc's volume density is radially exponential. Because we are interested here in the total mass density, we fitted an exponential to the surface brightness measured in ellipses with position angle and ellipticity fixed to the values determined from large radii. The fits to R_d started outside a_B ; we varied the radial range of the fits to obtain error estimates on R_d ; these were as large as 15 per cent. Variations in R_d are also included in our error estimate on $V_{\text{c,flat}}$.

With these assumptions, the asymmetric drift equation becomes

$$V_c^2 = V_*^2 + \frac{\sigma_{\text{obs}}^2}{\sin^2 i (1 + 2\alpha^2 \cot^2 i)} \left[2R \left(\frac{1}{R_d} + \frac{2}{R_\sigma} \right) - 1 \right]. \quad (2)$$

We apply this correction to all velocity data points (including those not on the major axis) outside the bar radius and within 30° of the major axis. We average over all these points to obtain $V_{\text{c,flat}}$, with an additional error from the scatter of the points added in quadrature. We report on our findings of $V_{\text{c,flat}}$ in Table 8, and in Fig. 8.

In Paper I, the high surface brightness of NGC 1023 allowed us to drop the assumption that $\sigma_\phi^2/\sigma_R^2 = \frac{1}{2}$, and instead we used the velocity dispersion data from all slits to obtain $V_{\text{c,flat}} = 270 \pm 31$ km s $^{-1}$ (having assumed $0.0 \leq \alpha \leq 1.0$; because of its high inclination $V_{\text{c,flat}}$ for this galaxy is not very sensitive to the value of α). For comparison, we have redone the asymmetric drift correction of NGC 1023 with the method described above for the new sample. We found $V_{\text{c,flat}} = 270 \pm 13$ km s $^{-1}$, which is in excellent agreement with the value of Paper I.

We finally measured \mathcal{R} as $V_{\text{c,flat}}/(a_B \Omega_p)$. We used Monte Carlo simulations to estimate the uncertainties in \mathcal{R} by varying $V_{\text{c,flat}}$ and a_B uniformly in their respective ranges, and varying Ω_p assuming the errors of Table 8 are Gaussian. We report the median and the 67 per cent interval of \mathcal{R} in Table 8.

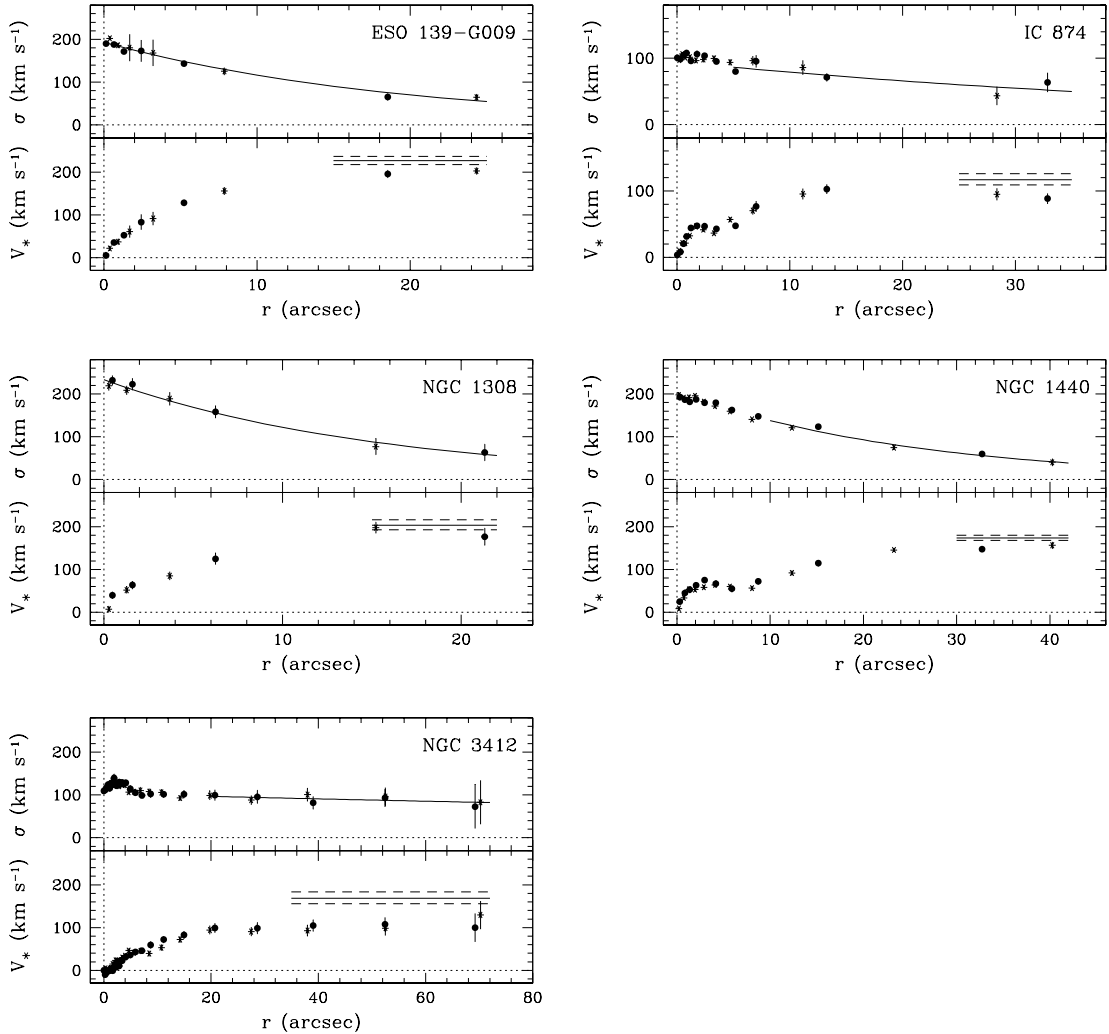


Figure 8. The major-axis radial profiles of the stellar line-of-sight velocity dispersion and velocity (after subtraction of the systemic velocity) of the sample galaxies. The profiles are folded around the centre. Filled dots and asterisks refer to receding and approaching sides of the galaxy, respectively. For each galaxy, the exponential radial profile fitting the line-of-sight velocity dispersion profile and circular velocity obtained by applying asymmetric drift correction are plotted in the upper and lower panels, respectively. Note that all data at $|\phi| \leq 30^\circ$ from all slits have been used for the fits to $V_{\text{c},\text{flat}}$, but only points on the major axis are shown in this figure.

7 DISCUSSION AND CONCLUSIONS

The five SB0s presented in this work, together with NGC 1023 studied in Paper I, which we include in our sample for this discussion, represent the largest sample of barred galaxies, with Ω_p measured by means of the TW method. For all of these, \mathcal{R} is consistent with being in the range 1.0–1.4, within the errors, i.e. with each having a fast bar. The unweighted average for the sample is $\bar{\mathcal{R}} = 1.1$. The apparent range of \mathcal{R} spans from 0.8 to 1.6 (0.6 to 2.1, within the 67 per cent intervals). This spread is not related to the properties of the galaxies in any obvious way (e.g. for the two galaxies at $V_{\text{c},\text{flat}} = 277 \text{ km s}^{-1}$, NGC 1023 and 1440, the measured values of \mathcal{R} are at opposite extremes of the distribution). The fact that some of the values of \mathcal{R} are nominally less than unity leads us to suggest that the large range of \mathcal{R} is a result of random errors and/or scatter in the measurements.

The sources of random errors are largely a result of measurement uncertainties in all three quantities used to compute \mathcal{R} , i.e. $V_{\text{c},\text{flat}}$, a_B and Ω_p . Of these, the largest is in Ω_p , amounting to typical fractional

uncertainties of 30 per cent, followed by a_B , for which the typical fractional uncertainty is 20 per cent. These uncertainties account for the typical large (and asymmetric towards large values) errors on measurements of \mathcal{R} .

A likely source of scatter is errors in the disc PA. Debattista et al. (2002, in progress) shows that, for PA errors of FWHM 5° (note that the root-mean-square PA uncertainty in our sample is 2.1°), the scatter in \mathcal{R} is of the order of 0.4, large enough to account for the $\mathcal{R} < 1$ cases. Because PA errors scatter \mathcal{R} to both larger and smaller values, then the largest measured value of $\mathcal{R} = 1.6$ is probably an overestimate. If this is the case, then the TW measurements find the same range of \mathcal{R} as do hydrodynamic simulations.

The conclusion that bars are fast constrains the dark matter distribution in disc galaxies. Debattista & Sellwood (1998, 2000) argued that bars this fast can only survive if the disc in which they formed is maximal. Recent high-resolution N -body simulations with cosmologically-motivated dark matter haloes have produced bars with \mathcal{R} in the range between 1.2 and 1.7 (Valenzuela & Klypin 2002). Even discounting our argument above in favour of a more

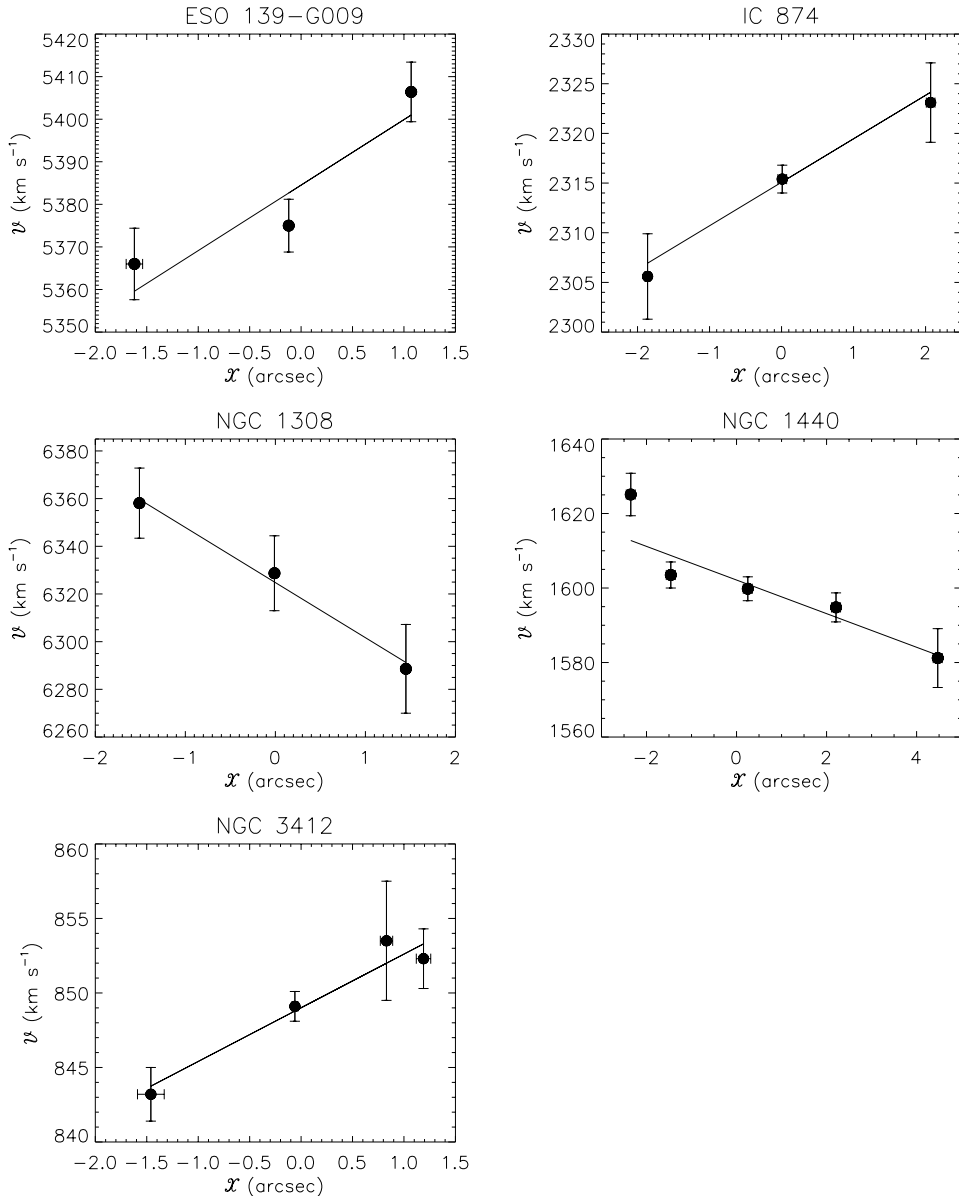


Figure 9. Pattern speed measurements for our sample of galaxies. The straight line is the best fit, with slope $\Omega_p \sin i$. The resulting values of Ω_p are given in Table 8.

restricted range of \mathcal{R} , Fig. 10 shows that $\mathcal{R} = 1.7$ is possible only for the bars of IC 874, NGC 1440, NGC 3412 and, marginally, NGC 936, while the bars of ESO 139-G009, NGC 1023, NGC 1308 and NGC 4596 never reach this value of \mathcal{R} . Note, moreover, that three of the galaxies that do reach $\mathcal{R} = 1.7$ have amongst the largest fractional errors in \mathcal{R} . Therefore we conclude that the N -body models of Valenzuela & Klypin (2002) probably produce slower bars than the observed.

The galaxy ESO 139-G009 is classified as SAB (i.e. weakly barred) in RC3; the fact that it hosts a fast bar suggests that weak bars form via the same mechanism that forms the strong ones. Thus, the hypothesis of Kormendy (1979), that weak bars are the end state of slowed down fast bars, already in question from N -body simulations (Debattista & Sellwood 2000), is also unsupported by the limited observational data. Further measurements of \mathcal{R} for weak bars would be of considerable interest.

ACKNOWLEDGMENTS

VPD and JALA acknowledge support by the Schweizerischer Nationalfonds through grant 20-64856.01. JALA was partially supported by Spanish DGC (Grant AYA2001-3939). EMC acknowledges the Astronomisches Institut der Universität Basel for the hospitality while this paper was in progress. We are indebted to R. Bender and R. Saglia for providing us with the FCQ package which we used for measuring the stellar kinematics. We are also grateful to A. Pizzella for the images he acquired. This research has made use of the Lyon-Meudon Extragalactic data base (LEDA) and of the NASA/IPAC Extragalactic data base (NED). This paper is based on observations carried out with the New Technology Telescope and the Danish 1.54-m Telescope (Prop. No 67.B-0230 and No 68.B-329) at the European Southern Observatory, La Silla (Chile), with the Italian Telescopio Nazionale Galileo (Prop. AOT-3, 3-06-119).

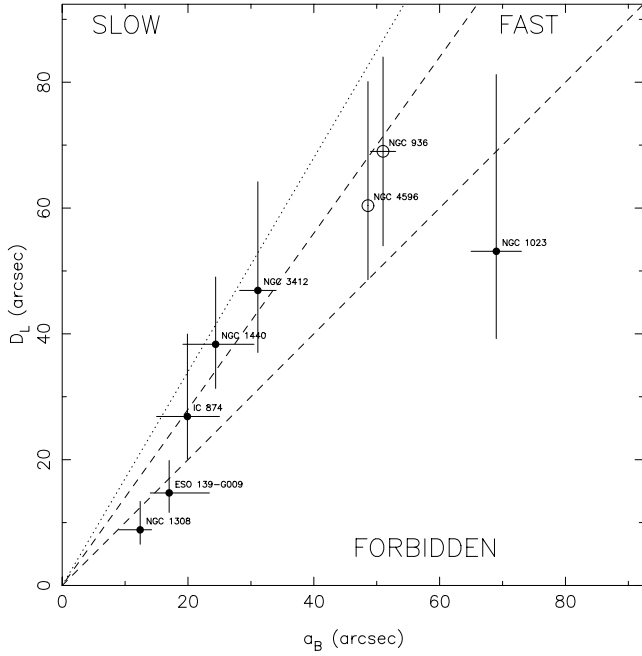


Figure 10. The corotation radius, D_L , and the bar semimajor axis, a_B , for the sample galaxies, including NGC 1023 (Paper I). The open circles represent galaxies which are not part of our sample: NGC 936 (Merrifield & Kuijken 1995) and 4596 (Gerssen et al. 1999). Dashed lines corresponding to $R = 1$ and $R = 1.4$, separate the fast-bar, slow-bar and forbidden regimes. The dotted line corresponds to $R = 1.7$.

operated on the island of La Palma by the Centro Galileo Galilei of the Consorzio Nazionale per l’Astronomia e l’Astrofisica, and with the Jacobus Kapteyn Telescope operated by the Isaac Newton group at La Palma island at the Spanish Observatorio del Roque de los Muchachos of the Instituto de Astrofísica de Canarias.

REFERENCES

- Aguerri J. A. L., Muñoz-Tuñón C., Varela A. M., Prieto M., 2000, A&A, 361, 841
 Aguerri J. A. L., Hunter J. H., Prieto M., Varela A. M., Gottesman S. T., Muñoz-Tuñón C., 2001, A&A, 373, 786.
 Ann H. B., 2001, Ap&SS, 276, 683
 Athanassoula E., 1992, MNRAS, 259, 345
 Athanassoula E., Misiriotis A., 2002, MNRAS, 530, 35
 Baggett W. E., Baggett S. M., Anderson K. S. J., 1998, AJ, 116, 1626
 Bender R., 1990, A&A, 229, 441
 Bender R., Saglia R. P., Gerhard O. E., 1994, MNRAS, 269, 785
 Binney J., Tremaine S., 1987, Galactic Dynamics, Princeton Univ. Press, Princeton
 Chapelon S., Contini T., Davoust E., 1999, A&A, 345, 81
 Contopoulos G., 1980, A&A, 81, 198
 Debattista V. P., Sellwood J. A., 1998, ApJL, 493, L5
 Debattista V. P., Sellwood J. A., 2000, ApJ, 543, 704
 Debattista V. P., Williams T. B., 2001, in Funes J. G., Corsini E. M., eds, ASP Conf. Ser. Vol. 230, Galaxy Disks and Disk Galaxies. Astron. Soc. Pac., San Francisco, p. 553
 Debattista V. P., Corsini E. M., Aguerri J. A. L., 2002, MNRAS, 332, 65
 Dehnen W., Binney J. J., 1998, MNRAS, 298, 387
 de Vaucouleurs G., de Vaucouleurs A., Corwin H. G., Buta R. J., Paturel G., Fouquè P., 1991, Third Reference Catalogue of Bright Galaxies. Springer-Verlag, New York (RC3)
 Duval M. F., Athanassoula E., 1983, A&A, 121, 297
 England M. N., Gottesman S. T., Hunter J. H., 1990, ApJ, 348, 456
 Faber S. M., Friel E. D., Burstein D., Gaskell C. M., 1985, ApJS, 57, 711
 Fisher D., 1997, AJ, 113, 950
 Freeman K. C., 1966, MNRAS, 133, 47
 Freeman K. C., 1970, ApJ, 160, 811
 Gerssen J., 2002, in Athanassoula E., Bosma A., eds, ASP Conf. Ser. Vol. 284, Disc of Galaxies: Kinematics, Dynamics and Perturbations. Astron. Soc. Pac., San Francisco, in press
 Gerssen J., Kuijken K., Merrifield M. R., 1997, MNRAS, 288, 618
 Gerssen J., Kuijken K., Merrifield M. R., 1999, MNRAS, 306, 926
 Gerssen J., Kuijken K., Merrifield M. R., 2000, MNRAS, 317, 545
 Hunter J. H., Ball R., Huntley J. M., England M. N., Gottesman S. T., 1989, ApJ, 324, 721
 Kent S. M., 1984, ApJS, 56, 105
 Kent S. M., 1985, ApJS, 59, 115
 Kent S. M., 1987, AJ, 93, 1062
 Kodaira K., Okamura S., Ichikawa S., 1990, Photometric Atlas of Northern Bright Galaxies. Univ. of Tokyo Press, Tokyo
 Kormendy J., 1979, ApJ, 227, 714
 Kuijken K., Fisher D., Merrifield M. R., 1996, MNRAS, 283, 543
 Laine S., 1996, PhD Thesis, Florida Univ.
 Lindblad P. A. B., Kristen H., 1996, A&A, 313, 733
 Lindblad P. A. B., Lindblad P. O., Athanassoula E., 1996, A&A, 313, 65
 Martin P., 1995, AJ, 109, 2428
 Merrifield M. R., Kuijken K., 1995, MNRAS, 274, 933
 Neistein E., Maoz D., Rix H.-W., Tonry J. L., 1999, AJ, 117, 2666
 Osterbrock D. E., Fulbright J. P., Martel A. R., Keane M. J., Trager S. C., Basri G., 1996, PASP, 108, 277
 Ohta K., Masaru H., Wakamatsu K., 1990, ApJ, 357, 71
 Press W. H., Teukolsky S. A., Vetterling W. T., Flannery B. P., 1992, Numerical Recipes, Cambridge Univ. Press, Cambridge
 Prieto M., Gottesman S. T., Aguerri J. L., Varela A., 1997, AJ, 114, 1413
 Prieto M., Aguerri J. A. L., Varela A. M., Muñoz-Tuñón C., 2001, A&A, 367, 405
 Sérsic J. L., 1968, Atlas de Galaxias Australes. Observatorio Astronómico, Córdoba
 Shaw M., Axon D., Probst R., Gatley I., 1995, MNRAS, 274, 369
 Tremaine S., Weinberg M. D., 1984, ApJ, 282, L5
 Valenzuela O., Klypin A., 2002, MNRAS, submitted
 van Albada T. S., Sanders R. H., 1982, MNRAS, 201, 303
 Weiner B. J., Sellwood J. A., Williams T. B., 2001, ApJ, 546, 931
 Wozniak H., Friedli D., Martinet L., Martin P., Bartschi P., 1995, A&AS, 111, 115

This paper has been typeset from a *T_EX/L_AT_EX* file prepared by the author.